Change Point Detection in Radar Reflectivity Measurements Contaminated by Speckle Noise

Sarah El Hajj Chehade, Hamza Issa, Georges Stienne, Serge Reboul

Change Point Detection in Radar Reflectivity Measurements Contaminated by Speckle Noise

Sarah El Hajj Chehade, Hamza Issa, Georges Stienne, and Serge Reboul

***Abstract*—This article studies the use of airborne global navigation satellite system reflectometry techniques for remote sensing applications at regional scale. The objective is to classify the reflectivity of airborne global navigation satellite system (GNSS) signals in order to differentiate various reflective surfaces along the satellite traces. For this purpose, we propose a segmentation algorithm based on an online change point detector and an offline change point localization estimate. Given the presence of speckle noise in GNSS signals, a homomorphic log-transformation is applied to mitigate this noise. In this context, the cumulative sum change point detector and the maximum likelihood change point localization are designed for a log-gamma distribution. We show that the proposed radar segmentation system is able to automatically detect different landforms along real flight experiments that took place in the northern region of France. Automatic classification using K-means clustering is applied to the segmented signals allowing to distinguish different segments of the signal.**

***Index Terms*—Airborne reflectivity, change point detection, change point localization, global navigation satellite system reflectometry (GNSS-R), homomorphic transformation, speckle noise.**

I. Introduction

THE advancement of global navigation satellite system (GNSS) has expanded the possibilities of remote sensing for Earth surface and atmosphere monitoring. By using refracted, reflected, and dispersed GNSS signals, data can be obtained from remote and inaccessible areas, offering global coverage and benefiting Earth observation purposes. The distinctive features of GNSS signals, including the use of L-band frequencies, make them particularly well-suited for remote sensing applications [1]. global navigation satellite system reflectometry (GNSS-R) is a bistatic radar system that uses the GNSS signals as "signals of opportunity" to characterize Earth surface.

Over the past few decades, GNSS-R has emerged as a reliable remote sensing technology [2] for its ability to measure essential surface parameters with high temporal resolution and wide coverage [3], [4]. GNSS-R receivers are capable of receiving both the direct signals from satellites and signals that are reflected from Earth surface. GNSS-R techniques can be applied in various applications depending on the type of surface being observed. It can estimate wind speed [5], [6], ocean salinity [7], and sea level altimetry [8], [9], and provide measurements of the cryosphere on land for sea ice detection [10], [11] and snow depth estimation [12], [13]. For land observation, GNSS-R applications involves mainly the measurement of soil moisture content [14], [15], assessment of plant biomass [16], and, more recently, the detection of in-land water bodies [17], [18]. In the near future, ESA plans to launch the HydroGNSS, which is a space-borne scout mission aimed to collect data on the hydrological climate variables of soil moisture content and to detect in-land water body surfaces using delay Doppler maps as observables. In existing literature, several works focus on the classification of radar signal traces using a per-pixel approach [19], [20], [21] for soil moisture estimation. These works typically employ a moving average window to smooth the signal. However, in these approaches, several parameters need to be tuned, and the reproducibility of the processing under various signal acquisition conditions is not guaranteed.

Remote sensing using GNSS-R can be adapted on a local scale using ground-based experiments and on a regional scale with airborne campaigns, which is the case in our application. Studies in [22] and [23] investigated the possibility of using airborne data collected by UAV-based GNSS-R sensors for water body surface measurement in support of flood monitoring operations. The use of UAVs expanded the capabilities of monitoring and characterizing a large water body surface with high precision. Our team has proposed in [17], a radar technique that uses airborne GNSS-R observations to detect in-land water body surfaces. The aim of the proposed approach is to detect, monitor, and characterize in-land water bodies in regions vulnerable to floods.

In GNSS-R remote sensing applications, the power of the reflected signal is localized at the specular point with respect to a given time. In this context, the observations are time series where changes indicate transitions between different reflecting surfaces. Accurate detection and localization of the points where the change has occurred, i.e., the border between two successive surfaces, are essential in such applications. In this regard, we can define, between two successive borders, a homogeneous area that can be classified and associated with a type of soil. For this purpose, change point detection algorithms are applied to airborne GNSS-R data. A change point within a dataset denotes a specific position through which a change or transition takes

Manuscript received 23 December 2023; revised 1 March 2024 and 3 May 2024; accepted 21 May 2024. Date of publication 5 June 2024; date of current version 17 June 2024. This work was supported by the CPER IDEAL program (approche Intégrée des Défis maritimes et Littoraux) for their financial support. *(Corresponding author: Sarah El Hajj Chehade.)*

The authors are with the Laboratoire d'Informatique, Signal et Image de la Côte d'Opale (LISIC), Université du Littoral Côte d'Opale (ULCO), 62228 Calais, France (e-mail: sarah.chehade@univ-littoral.fr; hamza.issa.10@gmail.com; georges.stienne@univ-littoral.fr; serge.reboul@univ-littoral.fr).

Digital Object Identifier 10.1109/JSTARS.2024.3410039

place in the statistical characteristics of the data. However, GNSS-R measurements encounters not only additive noise as was assumed in [17] but mainly multiplicative noise, i.e., speckle noise. Speckle noise, often found in remote sensing data, introduces a unique set of challenges due to its complex, granular nature [24].

We can find in the published works different statistical models for the speckle noise that are mainly used for the modeling of radar signals, SAR radar signals, and active and passive sonar. Most of these distributions are reviewed in [25]. Many different noise distributions have been studied in the literature, such as the log normal, Weibull, Fisher, and generalized gamma [26]. These distributions are empirical because they are not linked to the electromagnetic physical model of the scattering process. Other distributions such as Rayleigh, gamma, G^0, Rice, and the generalized Gaussian distribution were proposed according to physical models of the scattering radar process [25]. Each one of these distributions is adapted to a specific type of reflecting areas.

In our radar system, the reflectivity of the signal is defined as the ratio of the reflected signal intensity over the direct signal one. We assume that the area of reflection is homogeneous because the radar cross section is small. The altitude of the airborne GNSS-R receiver used in our flight experimentation is low (300 m) and the observations are obtained from satellites with high elevation angles. We show that the amplitude of the reflectivity is following a Rayleigh speckle model. As we consider the sum of several observations of intensity, the noise is distributed according to a gamma distribution.

Numerous published works extensively discuss reviews on sequential change point detection [27], [28], [29], where the noise is often characterized as Gaussian and additive. When the noise is multiplicative the problem is addressed with parametric approaches according to the noise distribution [30], [31]. Two different approaches of sequential change-point detection for a sequence of independent gamma distributed random variables, namely the maximum likelihood approach and the cumulative sum (CUSUM) control chart method, are mainly studied. In [32], a test was derived from the ratio of the likelihood function to detect change in the scale parameter of the gamma distribution. Fotopoulos et al. [33] proposed a methodology based on maximum likelihood estimate (MLE) to evaluate time series data with an unknown change point. A sharp approximation of the maximum of the log-likelihood was proposed in [34] to quickly detect change points in the gamma distributed time series. The authors in [35] and [36] derived the run-length distribution of CUSUM charts for gamma distributions and Tan et al. [37] studied the constancy and convergence rate of the CUSUM estimator for a negative associated sequence of random variables.

In both approaches, the performance of the change point detector depends on the gamma distribution parameters. We are indeed dealing with multiplicative noise, where the noise power is a function of the parameter values. In this context, the accuracy of the estimated likelihood, as well as the CUSUM probability of false alarm rate, are functions of the gamma distribution

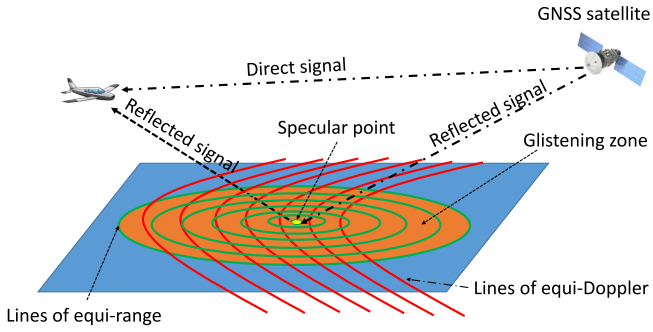

Fig. 1. GNSS-R system of observation.

shape and scale parameters. In practice, the reproducibility of the detection process is not guaranteed for these change point detection approaches because these parameters change over time.

In this article, we introduce a sequential change point detector designed within the statistical model of GNSS-R reflectivity. Our approach takes into account the presence of speckle noise, assumed to follow a gamma distribution. To fix the noise power, we employ a homomorphic log-transformation of the reflectivity, resulting in a log-gamma distribution with constant variance. The focus of change point detection is to estimate the time when a change occurs once detected, while sequential detection emphasizes identifying the change as soon as it takes place. In our approach, we use the CUSUM method along with a weighted moving average filter for sequential change detection in the log-transformed reflectivity. The threshold of the CUSUM algorithm is defined based on the average run length (ARL) ARL(0), a standard measure of the false alarm rate of a change point detector. When detecting a change, we use the MLE to determine the occurrence time, using the log-gamma distribution for processing. We classify the segmented radar signal with a classical K-mean approach. The classification allows to show that the different segments of the signal can be distinguished. The aim of this work is not to identify the nature of the reflecting surface. In an experimentation on real signals we show the reproducibility of the radar system's capability to differentiate reflecting surfaces using real flight data recorded by our team in northern France in 2020 and 2021.

The rest of this article is organized as follows. Section II introduces our proposed statistical model, based on the homomorphic transformation of the signal and the assumption of a gamma distribution. In Section III, we present a proposed estimation for the change point. The application of the proposed techniques to real flight experimentation is detailed in Section IV. Finally, Section VI concludes this article and discusses potential future research directions in this field.

II. Statistical Model of the GNSS-R Reflectivity

In a GNSS-R radar observation system (see Fig. 1), the reflectivity is processed as the ratio between the intensity of the reflected signal and the intensity of the direct signal from the GNSS satellite, as depicted. When the surface is flat, the

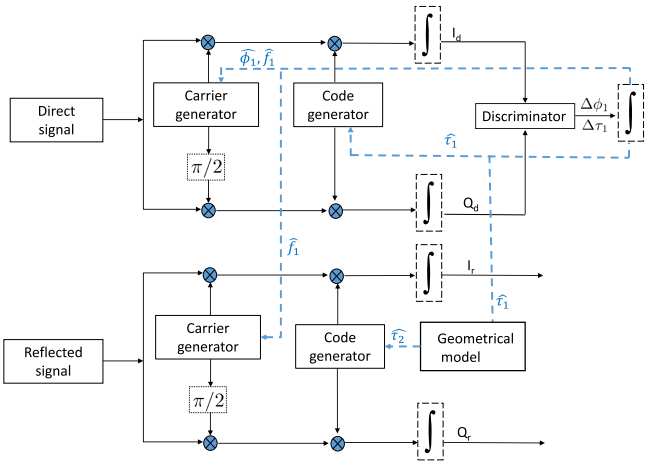

Fig. 2. Flowchart of the base-band receiver processing.

GNSS signal reflection primarily originates from the specular point, resulting in maximum reflected signal intensity. In contrast, for rough surfaces, signals reflected across the glistening zone reach the receiving antenna. Typically, the size of the glistening zone increases with surface roughness. In such cases, the scattered power comprises two components: a specular coherent component and an incoherent component due to surface roughness.

When a GNSS signal interacts with a rough surface, a noncoherent component of the reflected signal can be added, with a magnitude smaller than that of the coherent component and the power is scattered randomly in all directions. This implies that the level of coherency of the reflected signal is high for relatively smooth surfaces and low for very rough surfaces. Furthermore, within the glistening zones, numerous points provide reflected GNSS signals with Doppler and range parameters similar to the signal at the specular point. These points, where equirange and equi-Doppler lines intersect, generate multiple reflections with different phase delays that need to be considered in the GNSS signal processing model.

In this article, the receiver utilizes two tracking loops for the GNSS signal, each processing both the direct and reflected signals from every satellite. Fig. 2 illustrates the flow chart of the base-band signal processing following the downconversion and sampling of the direct signal (s_d) and reflected signal (s_r) from the GNSS satellites. Tracking of the direct signal employs traditional phase-locked loop (PLL) and delay-locked loop (DLL) techniques. Due to the dynamic nature of the GNSS-R receiver, frequency-locked loop (FLL) is also implemented to keep track of the changes in the Doppler frequency along the trajectory.

For the reflected signal, we employ an assisted loop that uses information from the direct signal. The assisted DLL loop uses the pseudorange of the direct signal and a geometric model to look at the delay of the specular reflected signal. The GNSS-R hardware receiver setup that we implement allows the assisted phase open loop of the reflected signal to use the Doppler frequency estimate obtained from the direct signal [17].

A. Direct Signal Tracking: PLL

After the demultiplexing stage, the direct signal processed by the PLL for each GNSS satellite can be represented as follows:

$$s_d(t) = a\,\sin\left(2\pi f_d t + \phi\right) + \eta \tag{1}$$

where a denotes the amplitude of the signal, f_d represents its Doppler, and η represents an additive noise component following a centred normal distribution. To process the correlation components of the signal, the following local replicas are generated:

$$s_l(t) = \sin\left(2\pi \hat{f}_1 t + \hat{\phi}\right) \tag{2}$$

$$c_l(t) = \cos\left(2\pi \hat{f}_1 t + \hat{\phi}\right) \tag{3}$$

where $\hat{f}_1$ and $\hat{\phi}$, respectively, represent the Doppler frequency and phase delay estimated by the FLL and the PLL. In its implementation, the DLL processes the following two correlation components:

$$I_d(\tau) = \int_0^{Tc} s_d(t) s_l(t+\tau) dt \tag{4}$$

$$Q_d(\tau) = \int_0^{Tc} s_d(t) c_l(t+\tau) dt \tag{5}$$

where $I_d(0)$ and $Q_d(0)$ represent the two quadrature components of correlation. Using these two correlation components, we calculate the signal intensity as

$$T_d = I_d^2(0) + Q_d^2(0) \tag{6}$$

$I_d(0)$ and $Q_d(0)$ are assumed to be random variables distributed according to the following Gaussian distributions:

$$I_d(0) \sim N(a\cos(\phi_e), \sigma^2) \tag{7}$$

$$Q_d(0) \sim N(a\sin(\phi_e), \sigma^2) \tag{8}$$

where $\phi_e = \phi - \hat{\phi}$ which is close to zero. The standard deviation, σ, of the Gaussian distribution is a function of the noise power in the direct signal. We can define the mean value of the direct signal intensity as

$$\frac{Td}{\sigma^2}$$

which follows a noncentral chi-squared distribution of parameter a^2. Then, we have

$$E(T_d) = a^2 + 2\sigma^2. \tag{9}$$

In our implementation, the direct signal is assumed to be stationary for large period of time, where its mean value is estimated.

B. Reflected Signal Tracking: Assisted Open Loop Phase Tracking

For the reflected signal, the demultiplexing stage is processed using the code delay of the direct signal, assuming the receiver's location is known. This operation is facilitated by an assisted

DLL, as described in [17]. After demultiplexing, the expression for the reflected signal is given by

$$s_r(t) = \sum_{i=1}^{L} a_i \sin\left(2\pi f_i t + \phi_i\right) + \eta \tag{10}$$

where a_i, f_i, and ϕ_i represent the parameters of the multiple reflections of the GNSS signal on the ground reaching the receiver antenna. L is the number of scatters on the reflecting surface. The assisted open loop tracking of the received signal processes the two quadrature components using the following replicas:

$$s_l(t) = \sin\left(2\pi \hat{f}_1 t\right) \tag{11}$$

$$c_l(t) = \cos\left(2\pi \hat{f}_1 t\right) \tag{12}$$

where $\hat{f}_1$ is the Doppler frequency estimate by the FLL of the direct signal tracking. The two quadrature components of correlation are defined as follows:

$$I_r(\tau) = \int_0^{Tc} s_r(t) s_l(t+\tau) dt \tag{13}$$

$$Q_r(\tau) = \int_0^{Tc} s_r(t) c_l(t+\tau) dt. \tag{14}$$

To process the intensity of the reflected signal, we use the component of correlation obtained for $\tau = 0$. In this context, the signal intensity, as a function of the two quadrature components, can be expressed as follows:

$$T = I_r^2(0) + Q_r^2(0). \tag{15}$$

The GNSS signal is reflected off a rough surface, and in this case the phases ϕ_i are assumed to be random following a uniform distribution between 0 and 2π according to the Goodman model [24]. Assuming that the central limit theorem is satisfied (i.e., L is large), the components of correlation are considered as random variables and are assumed to follow a centered normal distribution

$$I_r(0) \sim N\left(0, \sigma_r^2\right) \tag{16}$$

$$Q_r(0) \sim N\left(0, \sigma_r^2\right) \tag{17}$$

where the standard deviation σ_r is a function of the surface roughness. In our implementation, we process the mean intensity of the received signal within a working window of size N

$$T_r = \frac{1}{N}\sum_{i=1}^{N} T = \frac{1}{N}\sum_{i=1}^{N}\left(I_r^2(0) + Q_r^2(0)\right). \tag{18}$$

In this implementation, as we increase N, we enhance the signal-to-noise ratio (SNR) of the intensity. In practice for the GPS L1 signal, the components of correlation are processed with $Tc = 1\,ms$ data and a typical value of $N = 20$. From (15), (16), and (17), the intensity follows a gamma distribution:

$$T_r \sim \text{Gamma}\left(N, 2\sigma_r^2/N\right) \tag{19}$$

where $2\sigma_r^2$ is the mean value of the intensity and $4\sigma_r^4/N$ represents its variance.

C. Reflectivity of the GNSS-R Signal

In a GNSS-R radar system, both the direct signal from the satellite and the reflected signal obtained after the reflection of the direct signal on ground are observed. The power of the reflected signal is a function of the power of the direct signal. To normalize the observation of the reflected signal, we use the expression of reflectivity that is given by

$$R = \frac{T_r}{E(T_d)} = \frac{\frac{1}{N}\sum_{i=1}^{N}\left(I_r^2(0) + Q_r^2(0)\right)}{(a^2 + 2\sigma^2)} \tag{20}$$

where, $E(T_d)$, the mean intensity of the direct signal is considered constant during the duration of the experimentation. In practice, the intensity of the direct signal changes slowly over time and its mean value can be easily estimated.

In order to understand the meaning of R, the ideal coherent reflection is defined where the surface is flat and perfectly conductive, and the reflection is purely specular. The intensity of the reflected signal is maximum and its mean value $E(T_r)$ tends toward $E(T_d)$. Then, we have

$$E(R) = \frac{E(T_r)}{E(T_d)} \approx 1. \tag{21}$$

For the incoherent reflections, where we have multiple reflections of the direct signal due to the roughness of the surface, the mean value of the reflectivity is defined as

$$E(R) = \frac{E(T_r)}{E(T_d)} = \frac{2\sigma_r^2}{(a^2 + 2\sigma^2)}. \tag{22}$$

In this case, the intensity of the reflected signal is dispersed and $E(T_r) < E(T_d)$. Finally, we have

$$0 < E(R) < 1. \tag{23}$$

D. Homomorphic Transformation of the Signal

In this article, the reflectivity R is assumed to follow a gamma distribution, based on (19) and (20), and in accordance with the Goodman model [24], [38]. In this case, the noise on the observations is a multiplicative speckle noise. Let

$$R(N, \lambda) \sim \text{Gamma}\left(N, \lambda/N\right) \tag{24}$$

with

$$E(R(N,\lambda)) = \lambda = \frac{2\sigma_r^2}{(a^2 + 2\sigma^2)}. \tag{25}$$

In the case of a multiplicative model, the noise power is a function of the signal amplitude that varies in our application with the surface of reflection. The homomorphic log-operation transforms the multiplicative noise into additive noise, with constant noise power. The offset log-transform is defined by

$$W(N, \lambda) = \log\left(R(N, \lambda)\right) \tag{26}$$

with

$$W(N, \lambda) \sim \text{Log} - \text{Gamma}\left(N, \lambda/N\right) \tag{27}$$

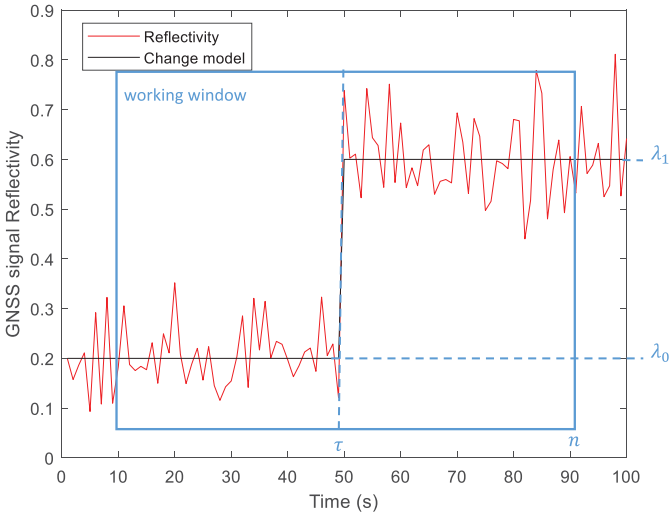

Fig. 3. Signal model in a working window.

where $V(W(N,\lambda))$, the variance of $W(N,\lambda)$, is constant. We have the following expressions:

$$E(W(N,\lambda)) = \Psi(N) + \log(\lambda/N) \tag{28}$$

$$V(W(N,\lambda)) = \Psi^{(1)}(N) \tag{29}$$

where $\Psi(\dots)$ and $\Psi^{(1)}(\dots)$ are, respectively, the digamma function and the trigamma function [39], [40].

III. Change Point Detection

In our radar application, a large amount of data is available, and we need to process these data sequentially as a chronological series. This series is considered to be in control when the statistical parameters of the process are stationary. In contrast, it is considered out of control in the nonstationary case when there is a change in the process. In this context, the hypothesis test for the change point detection can be defined as follows:

$$H_0 : R_t \sim \text{Log} - \text{Gamma}(N, \lambda_0/N)\, \forall t \in \{1, \dots, n\} \tag{30}$$

$$\begin{aligned} H_\tau &: R_t \sim \text{Log} - \text{Gamma}(N, \lambda_0/N)\, \forall t \in \{1, \dots, \tau\} \\ &: R_t \sim \text{Log} - \text{Gamma}(N, \lambda_1/N)\, \forall t \in \{\tau+1, \dots, n\} \end{aligned} \tag{31}$$

with $\lambda_0 \neq \lambda_1$ and $\tau \in \{1, \dots, n-1\}$, the instant of the change.

Fig. 3 represents the signal and its parameters under H_τ in the working window N. We can observe the increasing evolution of the signal model between the mean values λ_0 and λ_1 associated to the satellite footprint displacement from one area to another.

A. Proposed Change Point Detector

The main objective of the proposed detector is to detect a change in the observed process. Fig. 4 illustrate the flow chart of the proposed online/offline change point detector. As described in Fig. 4, the localization of the change is processed in a second step within a working window centered on τ', the detected instant of change.

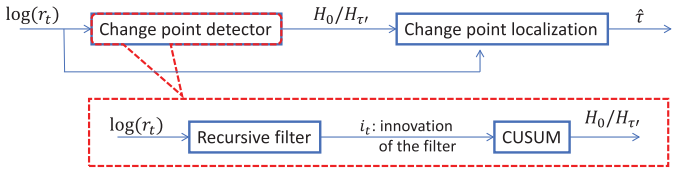

Fig. 4. Change detection system.

The filter can be defined as a recursive mean estimate derived from the log-transformation of the reflectivity observations

$$\bar{w}_t = \bar{w}_{t-1} + \frac{1}{K}\left(\log(r_t) - \bar{w}_{t-1}\right) \tag{32}$$

where K is the size of the window used to estimate the mean $\bar{w}_t$. In practice, K is a parameter that increases with time and removes information provided by the observation r_t. This estimate can be expressed as a weighted sum

$$\begin{aligned} &\bar{w}_t = \alpha_{1,t}\, \bar{w}_{t-1} + \alpha_{2,t}\, \log(r_t) \\ &\text{with } \alpha_{1,t} + \alpha_{2,t} = 1 \\ &\text{and } \alpha_{1,t} = 1 - \frac{1}{K},\ \alpha_{2,t} = \frac{1}{K}. \end{aligned} \tag{33}$$

This can be rewritten as

$$\bar{w}_t = \bar{w}_{t-1} + \alpha_{2,t}\, i_t \tag{34}$$

$$\text{with } i_t = \log(r_t) - \bar{w}_{t-1} \tag{35}$$

where i_t is the innovation of the filter. In the framework of optimal adaptive filtering [41], the optimal expression of $\alpha_{2,t}$ can be derived in the following recursive form:

$$P_t = \frac{(P_{t-1} + Q)\, \Psi^{(1)}(N)}{P_{t-1} + Q + \Psi^{(1)}(N)} \tag{36}$$

$$\alpha_{2,t} = \frac{P_t}{\Psi^{(1)}(N)} \tag{37}$$

where Q is a parameter defined by the user, and P_t the variance of the estimate $\bar{w}_t$. In this recursive form, $\alpha_{2,t}$ decreases with time toward a constant value, and the smoothing of the mean estimate increases until a constant smoothing level.

We can define the normalized innovation as

$$\tilde{i}_t = \frac{i_t}{P_{t-1} + \Psi^{(1)}(N)} \tag{38}$$

and the CUSUM detector in its simple form

$$g_t^+ = \left(g_{t-}^+ + \tilde{i}_t\right)^+ \tag{39}$$

$$g_t^- = \left(g_{t-}^- - \tilde{i}_t\right)^+ \tag{40}$$

$$\tau' = \min\left\{k : (g_t^+ \geq C_s) U (g_t^- \geq C_s)\right\} \tag{41}$$

where $(X)^+ = \max(X, 0)$. In the case of an innovation process, g_k^+ and g_k^-, the integration of the innovation process, evolves as a random walk before the change. After the change instant $\tau + t$, g_k^+, and g_k^- are monotonic increasing function.

The threshold C_s, fixed by the user, defines the probability of false alarm under H_0. However, the threshold C_s also determines the delay between the instant where the change occurred and the

instant an alarm is raised under H_τ. In our approach, this delay is corrected by the proposed change point estimate described in the next section.

B. Proposed Change Point Estimate

The samples $w_t = \log(r_t)$, where r_t are the observations of reflectivity, follow a log-gamma distribution $f(W_t; N, \lambda/N)$

$$f(W_t; N, \lambda/N) = \frac{(e^{W_t})^N e^{-\frac{N e^{W_t}}{\lambda}}}{(\frac{\lambda}{N})^N \Gamma(N)} \tag{42}$$

for $W_{1:n} = (W_1, \ldots, W_n)$, n i.i.d. samples distributed according to the log-gamma(N,λ/N) distribution. The n samples define the working window described in Fig. 3. We express the associated log-likelihood function $l(W_{1:n}; N, \lambda/N)$ as follows:

$$l(W_{1:n}; N, \lambda/N) = N \sum_{i=1}^{n} W_i - \frac{N}{\lambda} \sum_{i=1}^{n} e^{W_i} - nN \log\left(\frac{\lambda}{N}\right) - n \log(\Gamma(N)). \tag{43}$$

An estimate of λ can be defined by

$$\hat{\lambda} = N e^{(\overline{W} - \Psi(N))} \tag{44}$$

where

$$\overline{W} = \frac{1}{n} \sum_{i=1}^{n} W_i. \tag{45}$$

We can then define the generalized log-likelihood function as: $l(W_{1:n}; N, \hat{\lambda}/N)$ and estimate the localization of the change point τ by searching the following maximum log-likelihood:

$$\hat{\tau} = \underbrace{\operatorname{argmax}}_{0<\tau<n} \left[l\left(W_{1:\tau}; N, \hat{\lambda}_0/N\right) + l\left(W_{\tau+1:n}; N, \hat{\lambda}_1/N\right) \right] \tag{46}$$

where $\hat{\lambda}_0$ and $\hat{\lambda}_1$ are estimated with the samples $W_{1:\tau}$ and $W_{\tau+1:n}$, respectively.

C. Parameter Definitions

To ensure the reproducibility of the signals segmentation, the parameters of both the change point detector and change point estimate must be independent of the parameters and of the direct signal intensity (a and σ) and the reflected signal intensity (σ_r).

For the change point detector, we suggest fixing the threshold C_s as a function of the probability of false alarm rate. In change point detection, the false alarm rate is characterized by the ARL under H_0, denoted as ARL(0). ARL(0) is the expected number of observations between false alarms in a sequence of observations that represents noise without a change point. The value of ARL(0) is determined by simulation with a noise power $\sqrt{\Psi^{(1)}(N)}$ under H_0. The noise power defined by N is independent of the direct and reflected signal intensity.

The accuracy of the change point estimate relies only on the precision of estimating $\overline{W}$. This precision is determined by the noise power $\sqrt{\Psi^{(1)}(N)}$ and remains independent of the direct and reflected signal intensity.

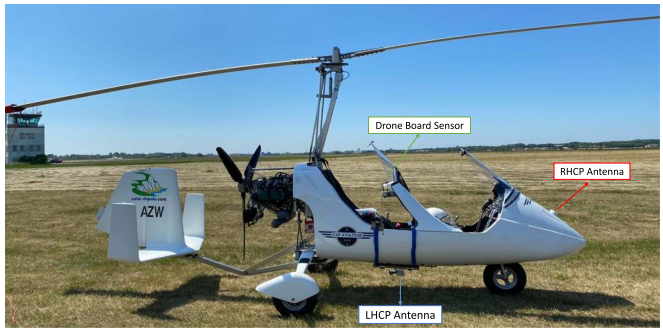

Fig. 5. Gyrocopter used during the flight experimentation with its sensors embedded on it.

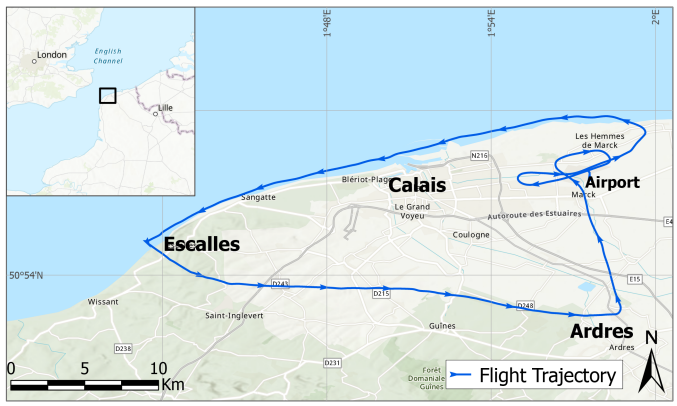

Fig. 6. Trajectory of both flights in the north of France.

IV. Experimentation: Application to Airborne GNSS-R Data

A. Flight Information

Airborne GNSS-R data was collected from two flights that took place in the northern region of France. **Flight 1** took place on October 19, 2020, starting at 14:45 Coordinated Universal Time (UTC). **Flight 2** took place on June 16, 2021, starting at 13:56 UTC. Fig. 5 shows the gyrocopter used, featuring various sensors embedded on it. The gyrocopter is equipped with a right-hand circular polarized antenna, positioned at the nose of the gyrocopter and oriented with a tilt of 40° from the zenith for the reception of the direct signals. A left-hand circular polarized antenna, embedded on the bottom and pointed toward the nadir, is responsible for receiving the reflected signals. The drone board sensor records the receiver attitude, altitude, and spatial coordinates which are essential for the localization of the GNSS measurements. In addition to the onboard sensors, the gyrocopter was equipped with the necessary components that constitute the GNSS-R hardware receiver for data collection.

Fig. 6 shows the trajectory of both flights. The gyrocopter took off from Calais–Dunkerque Airport. The flights duration lasted for approximately 45 min, covering an area of ≈230 km^2. The gyrocopter maintained an average speed of 95 km per hour during the course of both journeys, and it cruised at an average altitude of 315 m. The selection of this particular study area was motivated by its wide range of landforms.

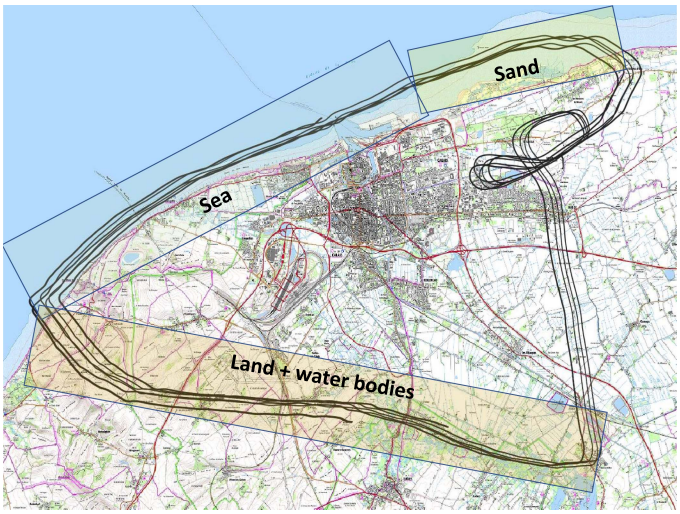

Fig. 7. Traces of the satellites with high elevation angles along the trajectory of Flight 1—October 19, 2020.

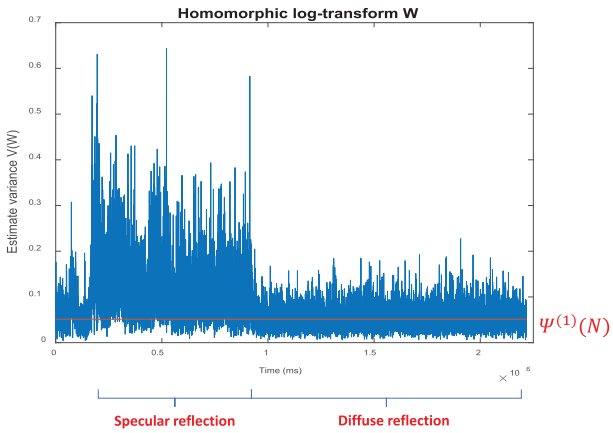

Fig. 8. Variance estimate of the homomorphic log-transform W.

In order to maximize the spatial resolution of our application, we analyze reflections from satellites with high elevation angles. The footprints of such satellites with cutoff elevation angle of 50°, are depicted in Fig. 7 for Flight 1. We scan a large zone of sandy beach, sea, and land including over 50 different in-land water body surfaces. The footprints traces are represented by 20 ms localization of the specular points of reflection.

B. Discussion of the Log Transform Noise Model

One of the main contributions of this article is to define an detection threshold that can be applied seamlessly to different sets of data. In our approach we assume that the log-transform of the reflectivity is distributed according to a log-gamma distribution. We can then define a detection threshold that is completely independent of the SNR because the standard deviation of the additive noise on the signal is fixed and known. In order to verify this assumption, we estimate the noise power on a set of real airborne GNSS-R reflectivity data, as depicted in Fig. 8.

Fig. 8 shows the variance of the reflectivity log-transform estimate on ten samples processed for the trace of satellite PRN 5. We can observe that the estimated variance is noisy.

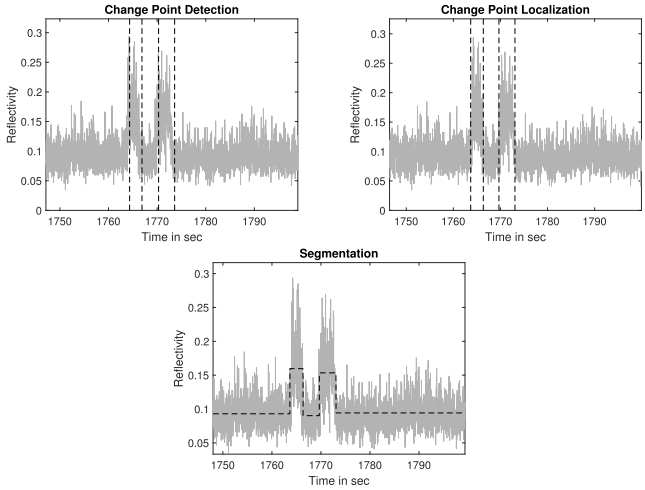

Fig. 9. Detection, localization, and segmentation process of an airborne GNSS signal reflectivity.

In this data, there are two sets of reflecting areas. The first is an area with specular reflections associated to reflections from sand and sea, and the second area with diffuse reflections associated to plain land. We show as a red line the theoretical variance of the log-transform of the reflectivity. This figure shows that this theoretical value is in accordance with the mean variance in the second area. Concerning the first area, the theoretical value underestimate the true value of the mean variance. In this case, the statistical model of the specular reflections is different from a gamma distribution.

The threshold is fixed for the land region where diffuse reflections exist. However, in areas characterized by coherent reflections from water surfaces, false alarm detection may increase due to the increase in the standard deviation of that specific area.

C. Change Point Estimation

In Fig. 9, we present the airborne reflectivity measurements acquired during our flight experimentation for two water bodies. The GNSS signal reflectivity variations, as shown in the following graphs, are detected and processed by a series of change detection algorithms.

Initially, the CUSUM algorithm detects changes in the reflectivity of the GNSS signal. In the CUSUM implementation, ARL(0) is fixed to 3000 for $\mathrm{N} = 20$ and the smoothing parameter $Q = 0.001$. In order to decrease the number of false alarms in the area of specular reflection the changes with a dynamic inferior to 0.01 are removed. Following the CUSUM detection, our proposed log-gamma maximum likelihood localization approach is applied to localize the changes as shown in Fig. 9. Finally, the signal is segmented into different sections associated to the change in the mean reflectivity levels based on the localized change point positions in Fig. 9.

D. Reflectivity Signal Segmentation

We apply our radar signal segmentation technique for in-land water body detection. Figs. 10 and 11 represent the radar signal segmentation for airborne GNSS measurements obtained along

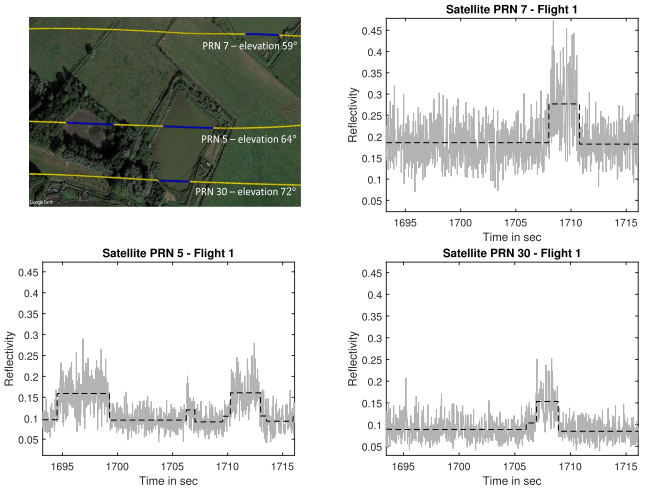

Fig. 10. Segmentation of the GNSS measurements—**Flight 1**.

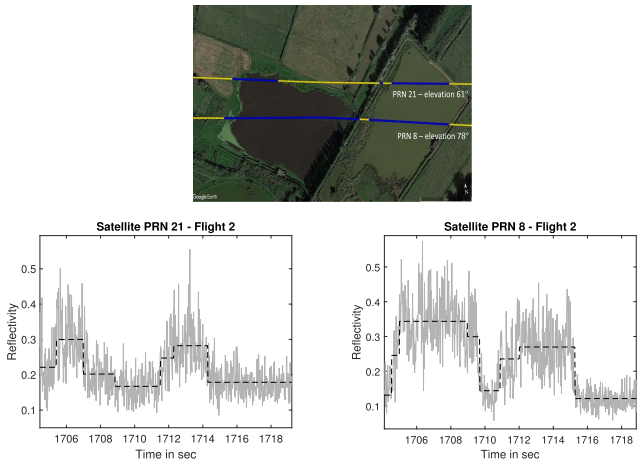

Fig. 11. Segmentation of the GNSS measurements—**Flight 2**.

the trajectories of both flights. The Google Earth images of these figures illustrate the traces of the satellite footprints represented by 20 ms localization of the specular points of reflection. It is color-coded—yellow denoting land and—blue indicating water bodies. These colors are associated to different mean reflectivity measurements. We also present the GNSS reflectivity measurements associated to each satellite signal along both flights and the corresponding signal segmentation with our proposed radar technique.

We analyze the GNSS measurements obtained from three different satellites (PRN 5, 7, and 30) of Flight 1 and two satellites (PRN 8 and 21) of Flight 2, each characterized by a different elevation angle. The surface reflectivity exhibits a direct correlation with the water content in land. The reflectivity measurements increase when the signals are reflected from a water body. In addition, the variance of the noise increases with the mean reflectivity.

We observe that the radar technique detects in-land water bodies with various sizes and shapes under different environments. We also show our system's capacity to utilize several datasets collected from different flights to automatically differentiate surfaces.

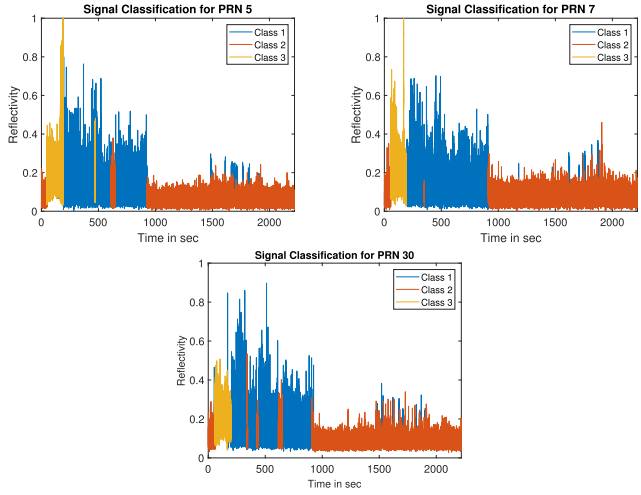

Fig. 12. Reflectivity classification for PRN 5, 7, and 30—**Flight 1**.

E. Automatic Classification of GNSS Signals Using K-Means Clustering

The statistical properties, i.e., the mean and standard deviation, of each segment are used to obtain a general classification of the signal using the K-means clustering technique.

The K-means approach is an effective unsupervised machine learning method that clusters data points based on the similarity of their features. In our study, it is important to note that each data point corresponds to a distinct segment of the reflectivity signal. The K-means method involves initialization, assignment, and update. K cluster centers are first initialized randomly. Segments are then assigned to the nearest cluster center based on their feature similarity, mean and standard deviation in our case. Then, the cluster centers are updated by calculating the mean values of the points inside each cluster. The iterative process continues until convergence is attained, usually when the distribution of segments to clusters achieves a state of stability.

In Fig. 12, our k-means segment clusters are depicted, illustrating three main classes corresponding to sandy beach, sea, and land when overlaid on visible (Google Earth) and IGN classification maps. We observe a significant level of stability in the segmentation results of Flight 1's three satellite signals under consideration. This demonstration showcases our segmentation approach ability to identify to three distinct classes, with an automatic categorization of the signal's characteristics with a general perspective on the nature of the GNSS-R data.

The same classification algorithm was applied to the reflectivity measurements obtained from PRNs 8 and 21 of Flight 2, and the corresponding results are presented in Fig. 13. The results are in alignment with those obtained from previous GNSS-R data, hence highlighting the reliability and consistency of the automatic classification approach across different datasets.

It is worth noting that there are differences in sea and sandy beach reflectivity levels between the two flights, attributed to a variety of factors, such as the difference in precipitation and wind

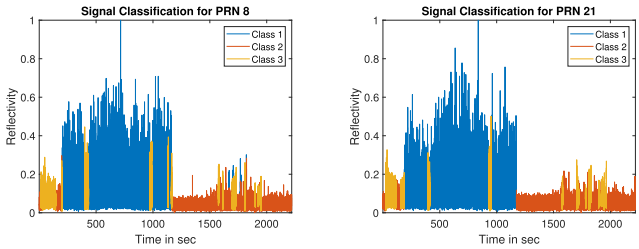

Fig. 13. Reflectivity classification for PRN 8 and 21—**Flight 2**.

speed between both flight dates. During the second flight, which was done on a day with clear weather conditions and relatively low wind speed, higher reflectivity measurements were obtained from the sea due to the reflections being mostly coherent, in contrast to Flight 1 where the presence of wind caused a decrease in the reflectivity levels due to a higher number of incoherent reflections.

V. Discussion

In our implementation, we use satellites with high elevation angles ranging from 59° to 78° to maximize signal power, ensuring a consistent impact within a range of 1dBiC. In addition, using satellites with high elevation angles maximize the spatial resolution of the application. Higher elevation angles results in a decreased satellite footprint size, which is crucial in airborne applications that use high-rate observations for the detection, differentiation, and especially the localization of the different areas of reflection.

An experiment was conducted to analyze how the elevation angle of a satellite affects the size of footprints, as represented by the major axis size of the first Fresnel zone of the reflecting area. The receiver height was kept constant at 315 m while the elevation angle varied from 30° to 90°. Results revealed a nearly exponential decrease in the major axis size as the elevation angle increased. Initially, at 30° elevation angle, the major axis size measured around 46 m. Subsequently, as the elevation angle increased, the major axis size decreased reaching approximately 19 m at 59° elevation, approximately 16 m at 78° elevation, and approximately 15.5 m at 90° elevation. This suggests that maintaining close elevation angles ensures consistent footprints on the soil, allowing for resolution consistency throughout flight experimentation. This stability in reflectivity change detection levels is supported by the consistent methodology employed across flights.

In addition, this approach helps mitigate variations in antenna patterns and their influence on reflectivity accuracy. The change point detection process employs a fixed threshold for detection across all flight traces, facilitating automatic segmentation.

Consequently, decreasing the elevation angle is unlikely to affect the change point detection as a process, although it may affect its accuracy. This is because lower elevation angles result in larger footprint sizes on the reflecting surface as previously mentioned, leading to reflectivity observations representing data from a broader area. In some cases, this surface can indeed be at the border between two different areas of reflection, causing notable fluctuations in reflectivity observations, particularly at the transition points. Ultimately, such variations can influence the accuracy of change detection. However, the extent of this influence depends on application preferences.

It is also worth noting that we are more concerned in the variations of the GNSS signal intensity. As we use a ratio of the direct and reflected signal intensity, affected by the same antenna pattern, the variations in the antenna pattern is of less importance in our application.

Furthermore, using the same antenna pattern for both direct and reflected signals minimizes the effect of antenna pattern variations on the detection of change in the levels of reflectivity.

The antennas used are commercial products from Antcom with references: G3Ant-53AT1-LH-RoHS and G3Ant-53AT1-RoHS. The calibration process is facilitated by our offline data processing workflow. The front end of our system comprises hardware components that downconvert and digitize the GPS signal. This hardware bit grabber is a commercial product from Syntony GNSS. To synchronize the digitization of signals from the direct and nadir antennas, the reflected signal is delayed using an optical fiber and summed with the direct signal at the front end's entrance. The receiver responsible for processing the data is a software-defined radio system developed by our team. This receiver, designed as a set of tools, sequentially processes signals from different satellites, ensuring accurate and reliable data processing.

During the analysis of reflectivity segmentation obtained for different PRNs across both flights, we observed a good agreement, indicating the effectiveness of our methodology. However, the automatic classification that uses the mean and the variance estimate in each segment is not sufficient to fully differentiate between sea and sand as shown for the different flights. During Flight 1, the wind speed was 24 km/h, whereas it was 12 km/h during Flight 2. This difference in wind speed helps explain why the reflectivity over the sea in Flight 1 is lower than in Flight 2. In addition, Flight 1 took place in October, a rainy month in northern France, which generally has high humidity. In contrast, Flight 2 was in June, a dry and warm month, contributing to the lower reflectivity levels of sand and land compared to Flight 1. In perspective of this work, environmental conditions as well as the measurement of coherence of the reflectivity should be able to improve the classification.

VI. Conclusion

In this article, we present change point detection and localization algorithms for the segmentation of GNSS-R reflectivity data. We consider such data as being affected by a gamma distributed, multiplicative speckle noise. In this case, the noise on the log of the reflectivity is shown to be additive, with constant variance only depending on the measurement sampling rate. A CUSUM change point detector and a maximum likelihood localization algorithm based on the log-transformation of the reflectivity observations are presented. The proposed radar system and statistical model demonstrate robust segmentation, even in the presence of speckle noise. Through real flight experiments conducted in the northern region of France, our algorithms show the ability to detect different landforms. Applying K-means

clustering for classification to the segmented signal enables us to distinguish different types of terrain. This study not only contributes to the field but also opens possibilities for future research, particularly in enhancing the classification technique for broader recognition of reflected surfaces.

ACKNOWLEDGMENT

The authors would like to thank the CPER IDEAL program (approche Intégrée des Défis maritimes et Littoraux) for their financial support.

REFERENCES

[1] K. Yu, C. Rizos, D. Burrage, A. G. Dempster, K. Zhang, and M. Markgraf, "An overview of GNSS remote sensing," *EURASIP J. Adv. Signal Process.*, vol. 2014, pp. 1–14, 2014.

[2] K. Yu et al., "Spaceborne GNSS reflectometry," *Remote Sens.*, vol. 14, no. 7, 2022, Art. no. 1605.

[3] Z. Li, F. Guo, F. Chen, Z. Zhang, and X. Zhang, "Wind speed retrieval using GNSS-R technique with geographic partitioning," *Satell. Navigation*, vol. 4, no. 1, pp. 4–18, 2023.

[4] J. L. Garrison and S. J. Katzberg, "The application of reflected GPS signals to ocean remote sensing," *Remote Sens. Environ.*, vol. 73, no. 2, pp. 175–187, 2000.

[5] J. L. Garrison, A. Komjathy, V. U. Zavorotny, and S. J. Katzberg, "Wind speed measurement using forward scattered GPS signals," *IEEE Trans. Geosci. Remote Sens.*, vol. 40, no. 1, pp. 50–65, Jan. 2002.

[6] E. Cardellach and A. Rius, "A new technique to sense non-Gaussian features of the sea surface from L-band bi-static GNSS reflections," *Remote Sens. Environ.*, vol. 112, no. 6, pp. 2927–2937, 2008.

[7] R. Sabia, M. Caparrini, A. Camps, and G. Ruffini, "Potential synergetic use of GNSS-R signals to improve the sea-state correction in the sea surface salinity estimation: Application to the SMOS mission," *IEEE Trans. Geosci. Remote Sens.*, vol. 45, no. 7, pp. 2088–2097, Jul. 2007.

[8] M. Martin-Neira, "A passive reflectometry and interferometry system (PARIS): Application to ocean altimetry," *ESA J.*, vol. 17, no. 4, pp. 331–355, 1993.

[9] S. Jin, X. Qian, and X. Wu, "Sea level change from BeiDou navigation satellite system-reflectometry (BDS-R): First results and evaluation," *Glob. Planet. Change*, vol. 149, pp. 20–25, 2017.

[10] M. B. Rivas, J. A. Maslanik, and P. Axelrad, "Bistatic scattering of GPS signals off arctic sea ice," *IEEE Trans. Geosci. Remote Sens.*, vol. 48, no. 3, pp. 1548–1553, Mar. 2010.

[11] J. Strandberg, T. Hobiger, and R. Haas, "Coastal sea ice detection using ground-based GNSS-R," *IEEE Geosci. Remote Sens. Lett.*, vol. 14, no. 9, pp. 1552–1556, Sep. 2017.

[12] E. Cardellach, F. Fabra, A. Rius, S. Pettinato, and S. D'Addio, "Characterization of dry-snow sub-structure using GNSS reflected signals," *Remote Sens. Environ.*, vol. 124, pp. 122–134, 2012.

[13] N. Rodriguez-Alvarez et al., "Snow monitoring using GNSS-R techniques," in *Proc. IEEE Int. Geosci. Remote Sens. Symp.*, 2011, pp. 4375–4378.

[14] S. J. Katzberg, O. Torres, M. S. Grant, and D. Masters, "Utilizing calibrated GPS reflected signals to estimate soil reflectivity and dielectric constant: Results from SMEX02," *Remote Sens. Environ.*, vol. 100, no. 1, pp. 17–28, 2006.

[15] B. W. Barrett, E. Dwyer, and P. Whelan, "Soil moisture retrieval from active spaceborne microwave observations: An evaluation of current techniques," *Remote Sens.*, vol. 1, no. 3, pp. 210–242, 2009.

[16] M. Zribi et al., "Performance of GNSS-R GLORI data for biomass estimation over the Landes forest," *Int. J. Appl. Earth Observation Geoinformation*, vol. 74, pp. 150–158, 2019.

[17] H. Issa, G. Stienne, S. Reboul, M. Raad, and G. Faour, "Airborne GNSS reflectometry for water body detection," *Remote Sens.*, vol. 14, no. 1, 2021, Art. no. 163.

[18] F. Frappart et al., "Automatic detection of inland water bodies along altimetry tracks for estimating surface water storage variations in the Congo Basin," *Remote Sens.*, vol. 13, no. 19, 2021, Art. no. 3804.

[19] Q. Yan, W. Huang, S. Jin, and Y. Jia, "Pan-tropical soil moisture mapping based on a three-layer model from CYGNSS GNSS-R data," *Remote Sens. Environ.*, vol. 247, 2020, Art. no. 111944.

[20] J. F. Munoz-Martin et al., "Single-pass soil moisture retrieval using GNSS-R at l1 and l5 bands: Results from airborne experiment," *Remote Sens.*, vol. 13, no. 4, 2021, Art. no. 797.

[21] J. F. Munoz-Martin, D. Llaveria, C. Herbert, M. Pablos, H. Park, and A. Camps, "Soil moisture estimation synergy using GNSS-R and L-band microwave radiometry data from FSSCat/FMPL-2," *Remote Sens.*, vol. 13, no. 5, 2021, Art. no. 994.

[22] R. Imam, M. Pini, G. Marucco, F. Dominici, and F. Dovis, "UAV-based GNSS-R for water detection as a support to flood monitoring operations: A feasibility study," *Appl. Sci.*, vol. 10, no. 1, 2019, Art. no. 210.

[23] A. Favenza, R. Imam, F. Dovis, and M. Pini, "Detecting water using UAV-based GNSS-Reflectometry data and artificial intelligence," in *Proc. IEEE Int. Workshop Metrol. Agriculture Forestry*, 2019, pp. 7–12.

[24] J. W. Goodman, "Statistical properties of laser speckle patterns," in *Laser Speckle and Related Phenomena*. Berlin, Germany: Springer, 1975, pp. 9–75.

[25] D. Yue, F. Xu, A. Frery, and Y. Jin, "SAR image statistical modeling : Part one–single-pixel statistical models," *IEEE Geosci. Remote Sens. Mag.*, vol. 9, no. 1, pp. 82–114, Mar. 2021.

[26] V. Krylov, G. Moser, S. B. Serpico, and J. Zerubia, "Modeling the statistics of high resolution SAR images," INRIA Research Rep. RR-6722, 2008.

[27] M. Basseville and I. V. Nikiforov, *Detection of Abrupt Changes: Theory and Application*. Englewood Cliffs, NJ, USA: Prentice-Hall, 1993.

[28] M. Csörgö and L. Horváth, "Limit theorems in change-point analysis," 1997.

[29] S. Aminikhanghahi and D. J. Cook, "A survey of methods for time series change point detection," *Knowl. Inf. Syst.*, vol. 51, pp. 339–367, 2016.

[30] D. V. Hinkley, "Inference about the change-point in a sequence of random variables," *Biometrika*, vol. 57, no. 1, pp. 1–17, 1970.

[31] J. Chen and A. Gupta, *Parametric Statistical Change Point Analysis: With Applications to Genetics, Medicine, and Finance*. Boston, MA, USA: Birkhäuser, 2012.

[32] D. Hsu, "Detecting shifts of parameter in gamma sequences with applications to stock price and air traffic flow analysis," *J. Amer. Stat. Assoc.*, vol. 74, pp. 31–40, 1979.

[33] S. B. Fotopoulos, A. Paparas, and V. K. Jandhyala, "Change point detection and estimation methods under gamma series of observations," *Stat. Papers*, pp. 1–32, 2022.

[34] X. Xiao, P. Chen, Z. Ye, and K.-L. Tsui, "On computing multiple change points for the gamma distribution," *J. Qual. Technol.*, vol. 53, no. 3, pp. 267–288, 2021.

[35] W. Huang, L. Shu, W. Jiang, and K.-L. Tsui, "Evaluation of run-length distribution for CUSUM charts under gamma distributions," *IIE Trans.*, vol. 45, no. 9, pp. 981–994, 2013.

[36] D. Jeske, "CUSUM algorithm for detecting translations in gamma distributions," *Qual. Rel. Eng. Int.*, vol. 32, pp. 1205–1211, 2016.

[37] C. Tan, B. Miao, and Z. Cai, "Statistical inference for the shape parameter change-point estimator in negative associated gamma distribution," *J. Inequalities Appl.*, vol. 2013, pp. 1–11, 2013.

[38] C. Oliver and S. Quegan, *Understanding Synthetic Aperture Radar Images*. Rijeka, Croatia: SciTech Publishing, 2004.

[39] L. J. Halliwell, "The log-gamma distribution and non-normal error," *Variance: Advancing Sci. Risk*, vol. 13, no. 2, pp. 173–189, 2021.

[40] R. L. Prentice, "A log gamma model and its maximum likelihood estimation," *Biometrika*, vol. 61, no. 3, pp. 539–544, 1974.

[41] M. Azmani, S. Reboul, J.-B. Choquel, and M. Benjemoul, "Un estimateur récursif des paramètres statistiques d'une distribution circulaire de von mises et d'une distribution log-normale. Application à l'estimation de la direction et de la vitesse du vent," *J. Européen des Systèmes Automatisés*, vol. 44, pp. 525–545, 2010.

Sarah El Hajj Chehade received the M.Sc. degree in signal, telecom, image, and speech processing from Lebanese University, Beirut, Lebanon, in 2022. She is currently working toward the Ph.D. degree in signal processing with the Laboratoire Signal et Image de la Côte d'Opale, University of the Littoral Opal Coast, Calais, France.

Her research interests include GNSS signal reflectometry and change point detection with applications to soil moisture analysis.

Hamza Issa received the Ph.D. degree in signal processing from the University of the Littoral Opal Coast, Calais, France, in 2022.

He then engaged in a postdoctoral program with Laboratoire Signal et Image de la Côte d'Opale, University of the Littoral Opal Coast, in partnership with Syntony GNSS, a French firm specializing in GNSS. He is currently a GNSS Tracking and Software Designer with Hexagon AB's Autonomy and Positioning Division, NovAtel Inc., Calgary, AB, Canada.

Georges Stienne received the M.Sc. degree in image and signal processing and the Ph.D. degree in signal processing from the University of the Littoral Opal Coast (ULCO), Calais, France, in 2010 and 2013 respectively.

He was a Postdoctoral with Purdue University, West Lafayette, IN, USA. Since 2015, he has been an Assistant Professor with ULCO. His research interests include statistical estimation of the parameters of multifrequencies global navigation satellite systems (GNSS) signals, with specific focus on phase processing through filtering, data fusion, and change point detection. He applies his works to GNSS positioning and GNSS-reflectometry.

Serge Reboul received the M.Sc. degree in telecommunication and the Ph.D. degree in signal processing from Lille University of Science and Technology, Villeneuve-d'Ascq, France, in 1991 and 1995, respectively.

He is currently an Associate Professor with the University of the Littoral Opal Coast, Calais, France. He has been applying his research in the field of GNSS since 2002 and has been working on the reflectometry of GNSS signals since 2007. His research interests include the fields of signal processing and information fusion.